

## Charge transfer across transition-metal oxide interfaces: Emergent conductance and electronic structure

Hanghui Chen,<sup>1,2</sup> Hyowon Park,<sup>1,2</sup> Andrew J. Millis,<sup>1</sup> and Chris A. Marianetti<sup>2</sup><sup>1</sup>*Department of Physics, Columbia University, New York, New York 10027, USA*<sup>2</sup>*Department of Applied Physics and Applied Mathematics, Columbia University, New York, New York 10027, USA*

(Received 31 July 2014; revised manuscript received 9 December 2014; published 22 December 2014)

We perform density functional theory plus dynamical mean-field theory calculations to investigate internal charge transfer in a superlattice composed of alternating layers of vanadate and manganite perovskite and Ruddlesden-Popper structure materials. We show that the electronegativity difference between vanadium and manganese causes moderate charge transfer from VO<sub>2</sub> to MnO<sub>2</sub> layers in both perovskite and Ruddlesden-Popper-based superlattices, leading to hole doping of the VO<sub>2</sub> layer and electron doping of the MnO<sub>2</sub> layer. Comparison of the perovskite and Ruddlesden-Popper-based heterostructures shows that apical oxygen motion in the perovskite superlattice enhances charge transfer. Our first principles simulations demonstrate that the combination of internal charge transfer and quantum confinement provided by heterostructuring is a powerful approach to engineering electronic structure and tailoring correlation effects in transition metal oxides.

DOI: [10.1103/PhysRevB.90.245138](https://doi.org/10.1103/PhysRevB.90.245138)

PACS number(s): 71.27.+a, 71.10.Fd, 74.72.-h, 74.78.Fk

### I. INTRODUCTION

Advances in thin film epitaxy growth techniques have made it possible to induce emergent electronic [1–10], magnetic [11–13], and orbital [14,15] states, which are not naturally occurring in bulk constituents, at atomically sharp transition-metal oxide interfaces [16–19]. For example, the interface between the two nonmagnetic band insulators LaAlO<sub>3</sub> and SrTiO<sub>3</sub> [4] has been reported to exhibit both conductance [20] and magnetism [21] (see reviews [22–25] and references therein). At the interface of Mott insulators SrMnO<sub>3</sub> and LaMnO<sub>3</sub>, hole doping on the Mn sites leads to rich phenomena, including metal-insulator transition, charge/spin/orbital ordering and magnetoresistance [26–28].

In LaAlO<sub>3</sub>/SrTiO<sub>3</sub> and related heterostructures, the interface electron gas is believed to be produced by the polar catastrophe mechanism, which leads to the transfer of charge from the sample surface to the interface. Here, we consider a different mechanism for controlling the electronic properties of an interface: namely, electronegativity-driven charge transfer. Recently, we have shown that internal charge transfer in a LaTiO<sub>3</sub>/LaNiO<sub>3</sub> superlattice transforms metallic LaNiO<sub>3</sub> into a  $S = 1$  Mott insulator and Mott-insulating LaTiO<sub>3</sub> into a  $S = 0$  band insulator [29]. A natural question arises: can we reverse the process and utilize internal charge transfer to induce conductance via oxide interfaces? In this regard, it is very tempting to explore Mott interfaces (one or both constituents are Mott insulators) due to the unusual phenomena (colossal magnetoresistance and high-temperature superconductivity) exhibited in certain doped Mott insulators.

In this paper we use density functional theory and dynamical mean-field theory (DFT+DMFT) to theoretically design a superlattice with emergent metallic behavior. We explore two different types of structure: the perovskite structure (referred to as 113-type) and the  $n = 1$  Ruddlesden-Popper structure (referred to as 214-type). Among the four bulk constituents (SrVO<sub>3</sub>, SrMnO<sub>3</sub>, Sr<sub>2</sub>VO<sub>4</sub>, and Sr<sub>2</sub>MnO<sub>4</sub>), all are correlation-driven insulators except SrVO<sub>3</sub>, which is a moderately correlated metal [30–32]. We show that the difference of electronegativity between the elements V and Mn drives

internal charge transfer from V to Mn sites, leading to a self-doping at the interface and possibly inducing conductance as Mn sites become weakly electron doped and V sites hole doped.

The rest of the paper is organized as follows: Sec. II presents the theoretical methods. A schematic of band alignment is presented in Sec. III to illustrate the underlying mechanism of charge transfer. All the bulk results from *ab initio* calculations are in Sec. IV and the results of vanadate-manganite superlattices are in Sec. V, both of which provide qualitative support and quantitative corrections to the schematic. The conclusions are in Sec. VI. Five Appendixes present technical details relating to the insulating gaps of Sr<sub>2</sub>VO<sub>4</sub> and Sr<sub>2</sub>MnO<sub>4</sub>, alternative forms of the double counting correction, LDA spectra of the superlattices and the possibility of two consecutive repeating layers (i.e., 2/2 superlattices instead of 1/1 superlattices).

### II. COMPUTATIONAL DETAILS

The DFT [33,34] component of our DFT+DMFT [35,36] calculations is performed using a plane-wave basis [37], as implemented in the Vienna *ab initio* simulation package (VASP) [38–41] using the projector augmented wave (PAW) approach [42,43]. Both local density approximation (LDA) [44] and Perdew-Burke-Ernzerhof generalized gradient approximation (GGA-PBE) [45] are employed. The correlated subspace and the orbitals with which it mixes are constructed using maximally localized Wannier functions [46] defined over the full 10 eV range spanned by the  $p$ - $d$  band complex, resulting in a well-localized set of  $d$ -like orbitals [47]. To find the stationary solution for our DFT+DMFT functional, we first find the self-consistent charge density within DFT. Subsequently we fix the charge density and converge the DMFT equations. A full charge self-consistency is not implemented in the present work. However, this approximation procedure is found to yield reasonable results in calculations of bulk systems [32,48,49].

For the bulk materials, we consider two structures: the experimental one and the theoretical relaxed structure obtained by the use of DFT. For the superlattice, we use DFT to

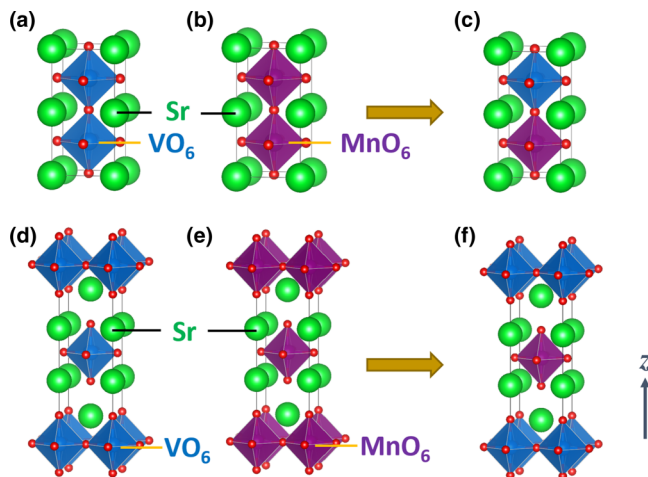


FIG. 1. (Color online) Simulation cells of (a) bulk SrVO<sub>3</sub>, (b) bulk SrMnO<sub>3</sub>, and (c) SrVO<sub>3</sub>/SrMnO<sub>3</sub> superlattice; (d) bulk Sr<sub>2</sub>VO<sub>4</sub>, (e) bulk Sr<sub>2</sub>MnO<sub>4</sub>, and (f) Sr<sub>2</sub>VO<sub>4</sub>/Sr<sub>2</sub>MnO<sub>4</sub> superlattice. The green atoms are Sr. The blue and purple cages are VO<sub>6</sub> and MnO<sub>6</sub> octahedra, respectively. The stacking direction of the superlattice is the [001] axis.

obtain the relaxed structure. We compare LDA and GGA calculations and both exchange correlation functions yield consistent results. The simulation cell is illustrated in Fig. 1. The stacking direction of the superlattice is along [001]. We use an energy cutoff of 600 eV. A  $12 \times 12 \times 12$   $[\frac{L_x}{L_z}]$  ( $L_x$  and  $L_z$  are the lattice constants along the  $x$  and  $z$  directions, and  $[x]$  is the integer part of  $x$ ) Monkhorst-Pack grid is used to sample the Brillouin zone. Both cell and internal coordinates are fully relaxed until each force component is smaller than 10 meV/Å and the stress tensor is smaller than 10 kBar. Convergence of the key results are tested with a higher energy cutoff (800 eV) and a denser  $k$ -point sampling  $20 \times 20 \times 20$   $[\frac{L_x}{L_z}]$  and no significant changes are found.

For the vanadates, we treat the empty  $e_g$  orbitals with a static Hartree-Fock approximation (recent work shows this approximation is adequate to describe the electronic structure of vanadates [32]), while correlations in the V  $t_{2g}$  manifold are treated within single-site DMFT including the Slater-Kanamori interactions using intraorbital Hubbard  $U_V = 5$  eV and  $J_V = 0.65$  eV [50–52]. For manganites, we treat the correlations on all the five Mn  $d$  orbitals within single-site DMFT using the Slater-Kanamori interactions with intraorbital Hubbard  $U_{Mn} = 5$  eV and  $J_{Mn} = 1$  eV [53]. The DMFT impurity problem is solved using the continuous time quantum Monte Carlo method [54–56]. In order to use the segment algorithm [57], we neglect the exchange and pairing terms in the Slater-Kanamori Hamiltonian. All the calculations are paramagnetic and the temperature is set to 232 K. Long-range magnetic ordering (in particular antiferromagnetism) might be induced at low temperature on Mn sites in manganites and in superlattices. A thorough study of magnetic properties will be presented elsewhere [58]. For the superlattice, we solve the problem in the single-site DMFT approximation, meaning that the self energy is site local and is one function on the V site and a different one on the Mn site. The self energies are determined from two quantum impurity models,

which are solved independently but coupled at the level of the self-consistency condition.

An important outstanding issue in the DFT+DMFT procedure is the double-counting correction, which accounts for the part of the Slater-Kanamori interactions already included in the underlying DFT calculation and plays an important role by setting the mean energy difference between the  $d$  and  $p$  bands. The  $p$ - $d$  separation plays a crucial role in determining the band alignment, which affects the charge transfer. However, currently there is no exact procedure for the double-counting correction. We use the  $U'$  double-counting method recently introduced [49], where the parameter  $U'$  is the prefactor in the double counting, which determines the  $p$ - $d$  separation and equivalently the number of electrons in the  $d$  manifold. In this study,  $U'$  is chosen to produce an energy separation between the O  $p$  and transition-metal  $d$  bands, which is consistent with photoemission experiments. Our main qualitative conclusions do not depend on the details of the double-counting scheme; in particular we show here they hold also for the conventional fully localized limit (FLL) double counting [59], which is the  $U' = U$  limit of the method of Ref. [49]. The reason is that in the superlattice, it is the relative V $d$ -Mn $d$  energy separation that controls the charge transfer. The FLL double-counting formula underestimates the  $p$ - $d$  separation in both SrVO<sub>3</sub> and SrMnO<sub>3</sub> by about 1 eV. However, such an error is canceled in the calculation of V $d$ -Mn $d$  energy separation. Therefore the FLL double counting does not change the charge transfer picture.

The spectral function presented throughout this work is defined as follows:

$$A_i(\omega) = -\frac{1}{\pi N_k} \sum_{\mathbf{k}} \text{Im}\{[(\omega + \mu)\mathbf{I} - H_0(\mathbf{k}) - \Sigma_{\text{tot}}(\omega) + V_{dc}]^{-1}\}_{ii}, \quad (1)$$

where  $i$  is the label of a Wannier function,  $N_k$  is the number of  $k$  points,  $\mathbf{I}$  is an identity matrix,  $H_0(\mathbf{k})$  is the DFT-LDA band Hamiltonian in the matrix form using the Wannier basis.  $\Sigma_{\text{tot}}(\omega)$  is the total self-energy and is understood as a diagonal matrix only with nonzero entries on the correlated orbitals. Local tetragonal point symmetry of the V and Mn sites ensures that  $\Sigma(\omega)$  is diagonal within the correlated orbital subspace.  $\mu$  is the chemical potential.  $V_{dc}$  is the double-counting potential, which is defined as [49]:

$$V_{dc} = (U' - 2J)(N_d - \frac{1}{2}) - \frac{1}{2}J(N_d - 3). \quad (2)$$

Note that if  $U' = U$ , then we restore the standard FLL double-counting formula [60]. For clarity, all the spectral functions presented in this paper are obtained from LDA+DMFT calculations. GGA+DMFT calculations yield qualitatively consistent results.

### III. SCHEMATIC OF BAND STRUCTURE AND BAND ALIGNMENT

We consider the following materials as components of the superlattice: SrVO<sub>3</sub>, a moderately correlated metal with nominal  $d$  valence  $d^1$ ; Sr<sub>2</sub>VO<sub>4</sub>, a correlation-driven insulator also with nominal valence  $d^1$ ; and SrMnO<sub>3</sub> and Sr<sub>2</sub>MnO<sub>4</sub>, both of which are  $d^3$  correlation-driven (Mott) insulators. Figure 1

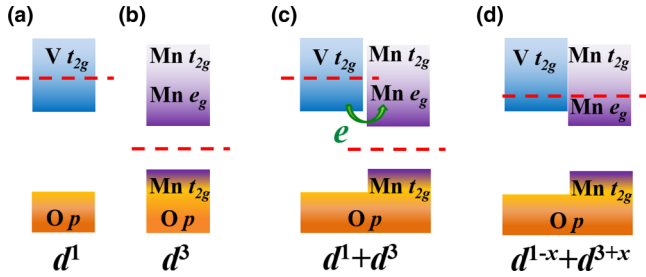


FIG. 2. (Color online) Schematic band structure of (a) vanadates and (b) manganites. (c) is the band alignment of the superlattice before the charge transfer occurs, i.e., two independent Fermi levels. (d) is the band structure of the superlattice after the charge transfer occurs, i.e., with one common Fermi level. The dashed red line denotes the Fermi level.

shows the atomic structure of the bulk phases of the constituent materials and the corresponding superlattices. Figures 1(a)–1(c) are bulk  $\text{SrVO}_3$ , bulk  $\text{SrMnO}_3$ , and  $\text{SrVO}_3/\text{SrMnO}_3$  superlattice, respectively. Figures 1(d)–1(f) are bulk  $\text{Sr}_2\text{VO}_4$ , bulk  $\text{Sr}_2\text{MnO}_4$ , and  $\text{Sr}_2\text{VO}_4/\text{Sr}_2\text{MnO}_4$  superlattice, respectively. In both superlattices, the stacking direction is along the [001] axis. In the 214-type, the V atoms are shifted by a  $(\frac{1}{2}, \frac{1}{2})$  lattice constant in the  $xy$  plane relative to the Mn atoms.

Figure 2 is a schematic of the band structure of bulk vanadates, bulk manganites, and the band alignments in the superlattice (the small insulating gap of  $\text{Sr}_2\text{VO}_4$  is not relevant here). There is a large energy separation (around 2 eV) between V  $d$  and O  $p$  states [see Fig. 2(a)]. In the Mn-based materials [see Fig. 2(b)], the highest occupied states are Mn  $t_{2g}$  derived and the lowest unoccupied states are Mn  $e_g$  derived. Due to the electronegativity difference between V and Mn, visible as the difference in the energy separation of the transition-metal  $d$  levels from the oxygen  $p$  levels, if we align the O  $p$  states between vanadates and manganites [see Fig. 2(c)], the occupied V  $t_{2g}$  states overlap in energy with the unoccupied

Mn  $e_g$  states. The overlap drives electrons from V sites to Mn sites. As the superlattice is formed, a common Fermi level appears across the interface and thus we expect that Mn  $e_g$  states become electron doped and V  $t_{2g}$  states hole doped.

We make two additional points: (i) though  $\text{SrVO}_3$  is a metal and  $\text{Sr}_2\text{VO}_4$  is an insulator with a small energy gap (around 0.2 eV) [30], the near-Fermi-level electronic structure does not affect the band alignment and therefore the internal charge transfer is expected to occur whether there is a small energy gap in V  $t_{2g}$  states at the Fermi level or not; (ii) in our schematic, we assume that the main peak of O  $p$  states are exactly aligned between the vanadates and manganites in the superlattices. Of course, real material effects will spoil any exact alignment. We will use *ab initio* calculations to provide quantitative information on how O  $p$  states are aligned between the two materials.

#### IV. BULK PROPERTIES

This section is devoted to properties of vanadates and manganites in their bulk single crystalline form. We perform DFT+DMFT calculations on both experimental structures and relaxed atomic structures obtained from DFT-LDA. The DFT-LDA relaxed V-O and Mn-O bond lengths, as well as the volume of  $\text{VO}_6$  and  $\text{MnO}_6$  octahedra, are summarized in Table I, along with the experimental bond lengths and octahedral volumes (in parentheses) for comparison. However, in order to directly compare to the photoemission data, we only present the spectral functions that are calculated using the experimental structures.

##### A. Bulk vanadates

We begin with bulk vanadates:  $\text{SrVO}_3$  and  $\text{Sr}_2\text{VO}_4$ .  $\text{SrVO}_3$  has a cubic structure with a lattice constant  $a = 3.841 \text{ \AA}$  [62].  $\text{Sr}_2\text{VO}_4$  forms  $n = 1$  Ruddlesden-Popper structure with the

TABLE I. The in-plane and out-of-plane V-O and Mn-O bond lengths  $l$  of  $\text{SrVO}_3$ ,  $\text{SrMnO}_3$ ,  $\text{Sr}_2\text{VO}_4$  and  $\text{Sr}_2\text{MnO}_4$ . The corresponding  $\text{VO}_6$  and  $\text{MnO}_6$  octahedral volumes  $\Omega$  are also calculated. The relaxed structures are obtained from DFT-LDA and DFT-GGA non-spin-polarized calculations. The experimental values, which are referenced in the main text, are also provided for comparison.

	$\text{SrVO}_3$			$\text{SrMnO}_3$			$\text{SrVO}_3/\text{SrMnO}_3$	
	LDA	GGA	exp	LDA	GGA	exp	LDA	GGA
$l_{\text{in}}(\text{V-O})$	1.89 $\text{\AA}$	1.93 $\text{\AA}$	1.92 $\text{\AA}$	–	–	–	1.88 $\text{\AA}$	1.92 $\text{\AA}$
$l_{\text{out}}(\text{V-O})$	1.89 $\text{\AA}$	1.93 $\text{\AA}$	1.92 $\text{\AA}$	–	–	–	1.85 $\text{\AA}$	1.88 $\text{\AA}$
$\Omega_{\text{VO}_6}$	9.00 $\text{\AA}^3$	9.59 $\text{\AA}^3$	9.44 $\text{\AA}^3$	–	–	–	8.72 $\text{\AA}^3$	9.24 $\text{\AA}^3$
$l_{\text{in}}(\text{Mn-O})$	–	–	–	1.86 $\text{\AA}$	1.90 $\text{\AA}$	1.90 $\text{\AA}$	1.88 $\text{\AA}$	1.92 $\text{\AA}$
$l_{\text{out}}(\text{Mn-O})$	–	–	–	1.86 $\text{\AA}$	1.90 $\text{\AA}$	1.90 $\text{\AA}$	1.89 $\text{\AA}$	1.94 $\text{\AA}$
$\Omega_{\text{MnO}_6}$	–	–	–	8.58 $\text{\AA}^3$	9.15 $\text{\AA}^3$	9.15 $\text{\AA}^3$	8.91 $\text{\AA}^3$	9.54 $\text{\AA}^3$
	$\text{Sr}_2\text{VO}_4$			$\text{Sr}_2\text{MnO}_4$			$\text{Sr}_2\text{VO}_4/\text{Sr}_2\text{MnO}_4$	
	LDA	GGA	exp	LDA	GGA	exp	LDA	GGA
$l_{\text{in}}(\text{V-O})$	1.88 $\text{\AA}$	1.92 $\text{\AA}$	1.91 $\text{\AA}$	–	–	–	1.85 $\text{\AA}$	1.90 $\text{\AA}$
$l_{\text{out}}(\text{V-O})$	1.96 $\text{\AA}$	2.00 $\text{\AA}$	1.95 $\text{\AA}$	–	–	–	1.93 $\text{\AA}$	1.95 $\text{\AA}$
$\Omega_{\text{VO}_6}$	9.24 $\text{\AA}^3$	9.83 $\text{\AA}^3$	9.49 $\text{\AA}^3$	–	–	–	8.81 $\text{\AA}^3$	9.39 $\text{\AA}^3$
$l_{\text{in}}(\text{Mn-O})$	–	–	–	1.82 $\text{\AA}$	1.86 $\text{\AA}$	1.90 $\text{\AA}$	1.85 $\text{\AA}$	1.90 $\text{\AA}$
$l_{\text{out}}(\text{Mn-O})$	–	–	–	1.99 $\text{\AA}$	2.04 $\text{\AA}$	1.95 $\text{\AA}$	1.99 $\text{\AA}$	2.06 $\text{\AA}$
$\Omega_{\text{MnO}_6}$	–	–	–	8.79 $\text{\AA}^3$	9.41 $\text{\AA}^3$	9.39 $\text{\AA}^3$	9.08 $\text{\AA}^3$	9.92 $\text{\AA}^3$

in-plane lattice constant  $a = 3.826 \text{ \AA}$  and the out-of-plane lattice constant  $c = 12.531 \text{ \AA}$  [63]. We use a Hubbard  $U_V = 5 \text{ eV}$  on both vanadate materials to include correlation effects on V  $d$  orbital. This value is similar to that used in previous studies [50–52].

Figure 3 shows the orbitally resolved spectral function  $A(\omega)$  of bulk SrVO<sub>3</sub> [Fig. 3(a)] and bulk Sr<sub>2</sub>VO<sub>4</sub> [Fig. 3(b)], along with the experimental photoemission data for bulk SrVO<sub>3</sub> [61]. The threshold of O  $p$  states is around 2 eV below the Fermi level. We find that  $U'_V = 3.5 \text{ eV}$  yields a reasonable agreement between the calculated O  $p$  states and experimental photoemission data. At  $U_V = 5 \text{ eV}$ , with the  $p$ - $d$  separation fixed by the experimental photoemission data, our DFT+DMFT calculations find SrVO<sub>3</sub> to be metallic, consistent with the experiment. However, they do not reproduce a Mott-insulating state in Sr<sub>2</sub>VO<sub>4</sub>, as observed in experiment. We show in Appendix A that a metal-insulator transition does occur in Sr<sub>2</sub>VO<sub>4</sub> with an increasing Hubbard  $U_V$  and a fixed  $p$ - $d$  separation (via  $U'_V$ ). However, the critical  $U_V$  is larger than typical values employed previously in literature for the vanadates [51,52]. It is possible that the experimentally observed narrow-gap insulating behavior (experimentally observed to persist above the Néel temperature [30,64]) arises from long-range magnetic correlations and spatial correlations that are not captured in our single-site paramagnetic DMFT calculation. These correlations relate to low-energy scale physics [65] and are not expected to affect the charge transfer energetics of interest here.

### B. Bulk manganites

Next we discuss the bulk manganites: SrMnO<sub>3</sub> and Sr<sub>2</sub>MnO<sub>4</sub>. For ease of comparison with the superlattice results to be shown in the next section, we study here the cubic phase of SrMnO<sub>3</sub> (isostructural to SrVO<sub>3</sub>) with the lattice constant of  $a = 3.801 \text{ \AA}$  (though other structures of SrMnO<sub>3</sub> also exist) [66]. Sr<sub>2</sub>MnO<sub>4</sub> forms in the  $n = 1$  Ruddlesden-Popper structure with in-plane and out-of-plane lattice constants  $a = 3.802 \text{ \AA}$  and  $c = 12.519 \text{ \AA}$  [67]. Consistent with the experimental estimation of Hubbard  $U$  from photoemission data [53], we use a Hubbard  $U_{Mn} = 5 \text{ eV}$  on both materials to include correlation effects on Mn  $d$  orbitals.

Figure 3 shows the orbitally resolved spectral function  $A(\omega)$  of bulk SrMnO<sub>3</sub> [Fig. 3(c)] and Sr<sub>2</sub>MnO<sub>4</sub> [Fig. 3(d)] [68]. The threshold of O  $p$  states is around 1 eV below the Fermi level. We find that  $U'_{Mn} = 4.5 \text{ eV}$  provides a good agreement between the calculated O  $p$  states and experimental photoemission data. We observe that for these parameters the occupied Mn  $t_{2g}$  states are visible as a peak slightly above the leading edge of the oxygen band. We will show in Appendix B that modest changes of parameters will move this peak slightly down in energy so that it merges with the leading edge of the oxygen  $p$  states. The experimental situation is not completely clear. Published x-ray photoelectron spectroscopy work [69,70] indicates a resolvable  $t_{2g}$  peak at or slightly above the leading edge of the oxygen bands; other studies including recent photoemission measurements [61,71] do not find a separately resolved  $t_{2g}$  peak. The issue is not important for the results of this paper but further investigation of the location of the  $t_{2g}$  states would be of interest as a way to refine our knowledge of the electronic structure of the manganites. With this value of  $U'_{Mn}$ , the theory produces a

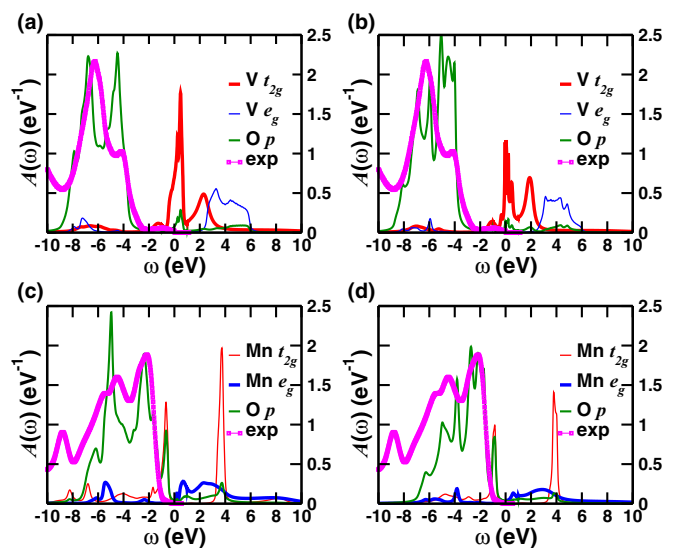


FIG. 3. (Color online) Orbitally resolved spectral function of (a) SrVO<sub>3</sub> and (b) Sr<sub>2</sub>VO<sub>4</sub>; (c) SrMnO<sub>3</sub> and (d) Sr<sub>2</sub>MnO<sub>4</sub>, obtained from LDA+DMFT calculations. The pink dots are the experimental spectra for either SrVO<sub>3</sub> or SrMnO<sub>3</sub> (identical data are plotted alongside the theoretical spectra for the Ruddlesden-Popper structures) [61]. For vanadates,  $U'$  double counting is employed with  $U_V = 5 \text{ eV}$  and  $U'_V = 3.5 \text{ eV}$ . The red (very thick), blue (thin), and green (thick) curves are V  $t_{2g}$ , V  $e_g$ , and O  $p$  projected spectral functions, respectively. For manganites,  $U'$  double counting is employed with  $U_{Mn} = 5 \text{ eV}$  and  $U'_{Mn} = 4.5 \text{ eV}$ . The red (thin), blue (very thick), and green (thick) curves are Mn  $t_{2g}$ , Mn  $e_g$ , and O  $p$  projected spectral functions, respectively. The Fermi level is set at zero energy.

small energy gap around 0.5 eV in both SrMnO<sub>3</sub> and Sr<sub>2</sub>MnO<sub>4</sub>. However, the gap value is  $U_{Mn}$  dependent. We show in Appendix B that with the  $p$ - $d$  separation fixed, via the adjustment of  $U'_{Mn}$ , a larger  $U_{Mn}$  increases the Mott gap by further separating the Mn lower and upper Hubbard bands. However, for the value of  $U_{Mn}$  (around 5 eV) that is extracted from photoemission experiments [53], the size of the Mott gap of Sr<sub>2</sub>MnO<sub>4</sub> is substantially underestimated, compared to the optical gap (around 2 eV) in experiment [30]. This discrepancy may arise because this calculation does not take into account spatial correlation [72]. However, the Mott gap is separated by Mn  $t_{2g}$  and  $e_g$  states, while the energy difference between O  $p$  states and Mn  $e_g$  states (i.e.,  $p$ - $d$  separation) is fixed by the experimental photoemission data (via  $U'_{Mn}$ ). We will show in the next section as well as in Appendix B that it is the  $p$ - $d$  separation that controls the charge transfer and therefore the underestimation of the Mott gap does not significantly affect our main results.

### V. VANADATE-MANGANITE SUPERLATTICES

In this section we discuss vanadate-manganite superlattices. There are two types: we refer to SrVO<sub>3</sub>/SrMnO<sub>3</sub> superlattice as 113-type and refer to Sr<sub>2</sub>VO<sub>4</sub>/Sr<sub>2</sub>MnO<sub>4</sub> superlattice as 214-type. The two types of superlattices have similarities and differences. In both types, the charge transfer from V sites to Mn sites occurs, in which electron dopes the Mn  $e_g$  states and drains the V  $t_{2g}$  states at the Fermi level. However, in the 214-type, the VO<sub>6</sub> and MnO<sub>6</sub> octahedra are decoupled and

the charge transfer arises mainly from the electronegativity difference between V and Mn elements. In the 113-type, in addition to the electronegativity difference between V and Mn, the movement of the shared apical oxygen changes the hybridization and thus also affects the charge transfer. We will show below that due to the movement of the shared apical oxygen atom, the 113-type superlattice generically has a more enhanced charge transfer than the 214-type superlattice.

We discuss the phenomena of charge transfer in terms of: (i) structural properties, (ii) electronic properties, and (iii) direct electron counting.

### A. Structural properties

Table I shows the DFT-LDA relaxed structure of SrVO<sub>3</sub>/SrMnO<sub>3</sub> and Sr<sub>2</sub>VO<sub>4</sub>/Sr<sub>2</sub>MnO<sub>4</sub> superlattices as well as the bulk materials. We see that the VO<sub>6</sub> octahedron is smaller in the superlattice than in the bulk, while the MnO<sub>6</sub> octahedron is larger. This is suggestive that the VO<sub>6</sub> octahedron loses electrons and the MnO<sub>6</sub> octahedron gains electrons (i.e., that internal charge transfer from V to Mn sites occurs), and this will be quantified below.

### B. Electronic properties

Figure 4 shows the orbitally resolved spectral function of the SrVO<sub>3</sub>/SrMnO<sub>3</sub> superlattice (left panels) and the Sr<sub>2</sub>VO<sub>4</sub>/Sr<sub>2</sub>MnO<sub>4</sub> superlattice (right panels). In both superlattices, the Mn  $e_g$  states emerge at the Fermi level, while in bulk manganites, there is a small gap in the Mn  $d$  states

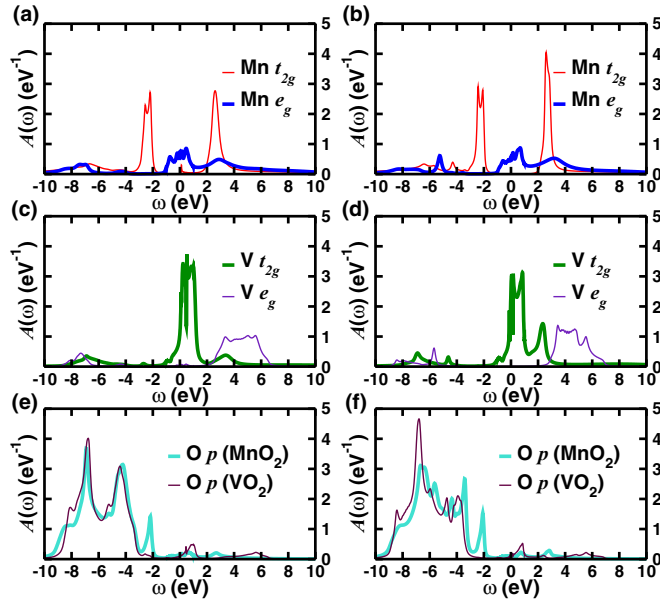


FIG. 4. (Color online) Orbitally resolved spectral function of vanadate-manganite superlattices, obtained from LDA+DMFT calculations. Left: SrVO<sub>3</sub>/SrMnO<sub>3</sub> superlattice. Right: Sr<sub>2</sub>VO<sub>4</sub>/Sr<sub>2</sub>MnO<sub>4</sub> superlattice. (a) and (b) Mn  $t_{2g}$  (red thin) and Mn  $e_g$  (blue thick) states; (c) and (d) V  $t_{2g}$  (green thick) and V  $e_g$  (violet thin) states; (e) and (f) O  $p$  states of the MnO<sub>2</sub> layer (turquoise thick) and O  $p$  states of the VO<sub>2</sub> layer (maroon thin).  $U'$  double counting is employed with  $U_V = U_{Mn} = 5$  eV and  $U'_V = 3.5$  eV,  $U'_{Mn} = 4.5$  eV. The Fermi level is set at zero point.

(separated by Mn  $e_g$  and  $t_{2g}$ ) in both materials. In the VO<sub>2</sub> layer, V  $t_{2g}$  states dominate at the Fermi level. Another feature worth noting is the O  $p$  states of the MnO<sub>2</sub> and of the VO<sub>2</sub> layers. Though the very first peak of O  $p$  states in the MnO<sub>2</sub> layer below the Fermi level is lined up with Mn  $t_{2g}$  states due to strong covalency, the main peak almost exactly overlaps with that of O  $p$  states in the VO<sub>2</sub> layer. This supports our hypothesis in the schematic that the main peaks of O  $p$  states of the VO<sub>2</sub> and MnO<sub>2</sub> layers are aligned in the superlattices. We need to mention that the general features in electronic structure of the superlattices are robust for different double-counting schemes. We show in Appendix C that the standard FLL double counting yields a very similar electronic structure of the superlattices. We also present LDA spectra in Appendix D for comparison to LDA+DMFT spectra.

Next, we compare the V  $t_{2g}$  and Mn  $e_g$  states between the superlattices and bulk materials to show how the Fermi level shifts in the two constituents. Figures 5(a) and 5(b) show the comparison of Mn  $e_g$  and O  $p$  states of the MnO<sub>2</sub> layer between the superlattices and bulk manganites [Fig. 5(a), 113-type and Fig. 5(b), 214-type]. The Fermi levels of bulk manganites and of the superlattices are lined up in the same figure.

According to the schematic (Fig. 2), with respect to bulk manganites, both the Mn  $d$  and O  $p$  states in the MnO<sub>2</sub> layer are shifted towards the low-energy-lying region due to the electron doping. Figures 5(a) and 5(b) clearly reproduce this rigid shift in (i) Mn  $e_g$  states from the bulk (blue or thin dark curves) to the superlattice (red or thick light) and (ii) in O  $p$  states of the MnO<sub>2</sub> layer from the bulk (turquoise or thin light) to the superlattice (maroon or thick dark).

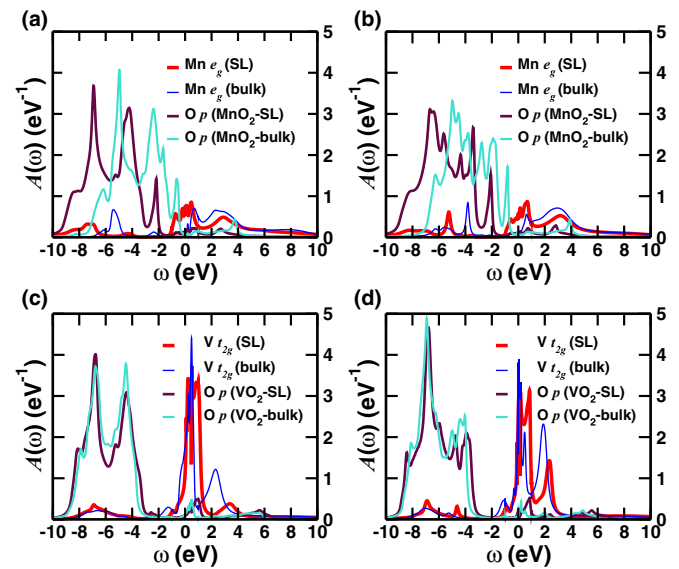


FIG. 5. (Color online) (a) Comparison of Mn  $e_g$  and O  $p$  states of the MnO<sub>2</sub> layer between the SrVO<sub>3</sub>/SrMnO<sub>3</sub> superlattice and bulk SrMnO<sub>3</sub>. (b) Comparison of Mn  $e_g$  and O  $p$  states of the MnO<sub>2</sub> layer between the Sr<sub>2</sub>VO<sub>4</sub>/Sr<sub>2</sub>MnO<sub>4</sub> superlattice and bulk Sr<sub>2</sub>MnO<sub>4</sub>. (c) Comparison of V  $t_{2g}$  and O  $p$  states of the VO<sub>2</sub> layer between the SrVO<sub>3</sub>/SrMnO<sub>3</sub> superlattice and bulk SrVO<sub>3</sub>. (d) Comparison of V  $t_{2g}$  and O  $p$  states of the VO<sub>2</sub> layer between the Sr<sub>2</sub>VO<sub>4</sub>/Sr<sub>2</sub>MnO<sub>4</sub> superlattice and bulk Sr<sub>2</sub>VO<sub>4</sub>. The Fermi level is set at zero energy. “SL” refers to the superlattices. All the spectra are obtained from LDA+DMFT calculations.

Similarly, Figs. 5(c) and 5(d) show the comparison of V  $t_{2g}$  and O  $p$  states (of the VO<sub>2</sub> layer) between the superlattices and bulk vanadates [Fig. 5(c), 113-type and Fig. 5(d), 214-type]. The Fermi levels of bulk vanadates and of the superlattices are lined up in the same figure. According to the schematic (Fig. 2), since electrons are drained out of V  $t_{2g}$  state, both the V  $t_{2g}$  states and O  $p$  states of the VO<sub>2</sub> layer are shifted towards the high-energy-lying region, compared to their counterparts in bulk vanadates. This shift can be seen [Figs. 5(c) and 5(d)] (i) in the V  $t_{2g}$  states from the bulk (blue or thin dark curves) to the superlattice (red or thick light) and (ii) in the O  $p$  states of the VO<sub>2</sub> layer from the bulk (turquoise or thin light) to the superlattice (maroon or thick dark). However, since the peak of V  $t_{2g}$  states at the Fermi level is much higher than that of Mn  $e_g$  states, the shift in the V  $t_{2g}$  states is much smaller than that in the Mn  $e_g$  states. Figure 5 reproduces our schematic of how V  $t_{2g}$  and Mn  $e_g$  states are shifted and rearranged to reach one common Fermi level in a vanadate-manganite superlattice. A possible consequence is electron (hole) conductance in the MnO<sub>2</sub> (VO<sub>2</sub>) layer.

### C. Direct electron counting

Now we calculate the occupancy on each orbital by performing the following integral:

$$N_i = \int_{-\infty}^{\infty} A_i(\omega) n_F(\omega) d\omega, \quad (3)$$

where  $A_i(\omega)$  is the spectral function for the  $i$ th orbital (defined from the Wannier construction), which is defined in Eq. (1).  $n_F(\omega)$  is the fermion occupancy factor. In order to explicitly display the charge transfer phenomenon, we calculate the V  $d$  and Mn  $d$  occupancy in both bulk materials and the superlattices. We summarize the results in Table II. We can see that  $N_d(\text{V})$  decreases and  $N_d(\text{Mn})$  increases from bulk to the superlattices and an average charge transfer from V to Mn is  $0.40e$  for the 113-type superlattice and  $0.25e$  for the 214-type superlattice. Moreover, due to the strong covalency between

transition-metal  $d$  states and oxygen  $p$  states, the occupancy of oxygen  $p$  states also changes between bulk materials and the superlattices. For this reason, the change in  $d$  occupancy may not be an accurate representation of charge transfer.

We also calculate the total occupancy of VO<sub>2</sub> and MnO<sub>2</sub> layers and find that the total charge transfer between the two layers amounts to  $0.53$  for the 113-type superlattice and  $0.38$  for the 214-type superlattice. Unlike the 113-type superlattice in which the apical oxygen is shared by two octahedra, the 214-type superlattice has a unique property that each octahedron is decoupled between layers. Therefore in the superlattice, we can count the charge transfer from the VO<sub>6</sub> octahedron to the MnO<sub>6</sub> octahedron. Note that since we only take into account the  $p$ - $d$  band manifold, the V and Mn octahedra include all the Wannier states and therefore in bulk Sr<sub>2</sub>VO<sub>4</sub>, the number of electrons per VO<sub>4</sub> unit is exactly  $25e$  and in bulk Sr<sub>2</sub>MnO<sub>4</sub>, the number of electrons per MnO<sub>4</sub> unit is exactly  $27e$ . We find that relative to the bulk materials, the V octahedron of the 214-type superlattice loses  $0.48e$  and Mn octahedron of the 214-type superlattice gains exactly  $0.48e$ . Comparison of this  $0.48e$  charge transfer to the  $0.25e$  found by only considering  $d$  orbitals further confirms that not only the transition-metal  $d$  states but also oxygen  $p$  states participate in the charge transfer. From Table II, we can see that the internal charge transfer is stronger in the 113-type superlattice, compared to the 214-type. We show below that the difference arises because in the 113-type superlattice, the apical oxygen is shared by the VO<sub>6</sub> and MnO<sub>6</sub> octahedra, whereas the octahedra are decoupled in the 214-type.

We see from Table I that due to the internal charge transfer, the VO<sub>6</sub> octahedron loses electrons and shrinks; on the other hand, the MnO<sub>6</sub> octahedron gains electrons and expands. Therefore the shared apical oxygen atom moves away from Mn sites and towards V sites [see Fig. 6(a)]. A direct consequence is that the out-of-plane Mn-O hopping decreases and the out-of-plane V-O hopping increases. Since the V  $d$  and Mn  $d$  states are antibonding in nature, the changes in the metal-ligand hopping push the V  $d$  states higher in energy and lower the

TABLE II. The occupancy of V  $d$  and Mn  $d$  states, as well as VO<sub>2</sub> and MnO<sub>2</sub> layers in vanadates, manganites and the superlattices. All the occupancies are calculated from Wannier basis using the DFT-LDA or DFT-GGA relaxed structures.  $\overline{\Delta N_d}$  ( $\overline{\Delta N}$ ) [73] is the average charge transfer between V  $d$  and Mn  $d$  states (VO<sub>2</sub> and MnO<sub>2</sub> layers, or VO<sub>4</sub> and MnO<sub>4</sub> octahedra), using the DFT-LDA relaxed structures.

SrVO <sub>3</sub>		SrMnO <sub>3</sub>		SrVO <sub>3</sub> /SrMnO <sub>3</sub>		charge transfer
LDA/GGA	LDA/GGA	LDA/GGA	LDA/GGA	LDA/GGA	LDA/GGA	LDA/GGA
$N_d(\text{V})$	$N_d(\text{Mn})$	$N_d(\text{V})$	$N_d(\text{Mn})$	$\overline{\Delta N_d}$		
2.09/2.01	4.08/4.05	1.73/1.59	4.51/4.57	0.40/0.47		
$N(\text{VO}_2)$	$N(\text{MnO}_2)$	$N(\text{VO}_2)$	$N(\text{MnO}_2)$	$\overline{\Delta N}$		
13.36/13.34	15.36/15.35	12.86/12.73	15.92/16.03	0.53/0.65		
Sr <sub>2</sub> VO <sub>4</sub>		Sr <sub>2</sub> MnO <sub>4</sub>		Sr <sub>2</sub> VO <sub>4</sub> /Sr <sub>2</sub> MnO <sub>4</sub>		charge transfer
LDA/GGA	LDA/GGA	LDA/GGA	LDA/GGA	LDA/GGA	LDA/GGA	LDA/GGA
$N_d(\text{V})$	$N_d(\text{Mn})$	$N_d(\text{V})$	$N_d(\text{Mn})$	$\overline{\Delta N_d}$		
2.07/2.00	4.12/4.11	1.86/1.71	4.41/4.44	0.25/0.31		
$N(\text{VO}_2)$	$N(\text{MnO}_2)$	$N(\text{VO}_2)$	$N(\text{MnO}_2)$	$\overline{\Delta N}$		
13.35/13.34	15.42/15.44	13.01/12.90	15.83/15.91	0.38/0.46		
$N(\text{VO}_4)$	$N(\text{MnO}_4)$	$N(\text{VO}_4)$	$N(\text{MnO}_4)$	$\overline{\Delta N}$		
25.00/25.00	27.00/27.00	24.52/24.42	27.48/27.58	0.48/0.58		

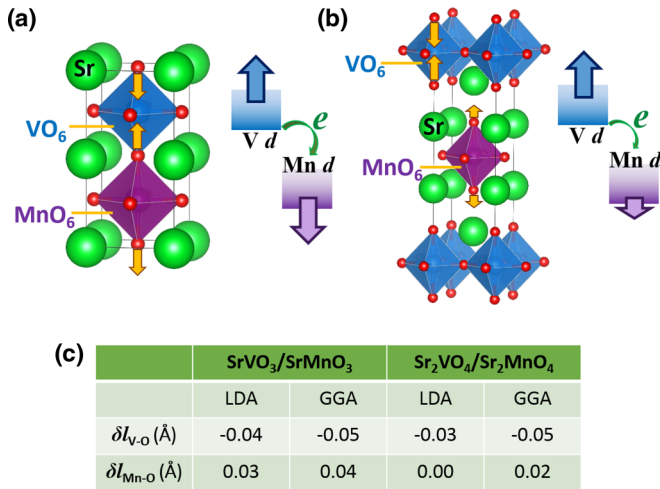


FIG. 6. (Color online) Movement of the apical oxygen, corresponding changes in the energy of V  $d$  and Mn  $d$  states and enhancement of the charge transfer. (a) SrVO<sub>3</sub>/SrMnO<sub>3</sub> superlattice and (b) Sr<sub>2</sub>VO<sub>4</sub>/Sr<sub>2</sub>MnO<sub>4</sub> superlattice. The green atoms are Sr. The blue and purple cages are VO<sub>6</sub> and MnO<sub>6</sub> octahedra, respectively. The arrows on the oxygen atoms indicate the atom movement. The arrows on the metal  $d$  states indicate the trend of energy shift. The length of the arrows is schematically proportional to the magnitude. (c) Table of the changes of out-of-plane V-O and Mn-O bonds ( $\delta l_{V-O}$  and  $\delta l_{Mn-O}$ ) from bulk materials to the superlattices.

energy of Mn  $d$  states and thus enhance the internal charge transfer. In the 214-type superlattice, we have a different situation because the two oxygen octahedra have their own apical oxygen atoms, whose movements are decoupled. From the Table I and Fig. 6(c), the VO<sub>6</sub> shrinks and the apical oxygen atom of VO<sub>6</sub> moves towards the V atom, just like the 113-type superlattice. However, the MnO<sub>6</sub> expands but the movement of apical oxygen is much smaller (the in-plane Mn-O bond does increase, so does the overall volume of MnO<sub>6</sub>). Therefore, the energy of V  $d$  states is increased due to the enhanced out-of-plane V-O hopping, but the energy of Mn  $d$  states does not decrease much because the movement of apical oxygen atom is reduced [Fig. 6(b)]. As a result, the charge transfer between V and Mn sites is weaker in the 214-type superlattice, compared to the 113-type superlattice.

Our discussions in this paper have focused mainly on the (SrVO<sub>3</sub>)<sub>1</sub>/(SrMnO<sub>3</sub>)<sub>1</sub> superlattice. Though  $m = 1$  superlattices [in the notation of (SrVO<sub>3</sub>) <sub>$m$</sub> /(SrMnO<sub>3</sub>) <sub>$m$</sub> ] are easy for theoretical studies, experimentally it is more practical to grow  $m = 2$  or larger  $m$  superlattices. We show in Appendix E that comparing (SrVO<sub>3</sub>)<sub>1</sub>/(SrMnO<sub>3</sub>)<sub>1</sub> and (SrVO<sub>3</sub>)<sub>2</sub>/(SrMnO<sub>3</sub>)<sub>2</sub> superlattices, the charge transfer is very similar. However, for a large  $m$ , we will have inequivalent V sites and eventually the charge transfer will be confined to the interfacial region. Investigating the length scales associated with charge transfer is an important open question.

## VI. CONCLUSIONS

We use DFT+DMFT calculations to show that due to the difference in electronegativity, internal charge transfer

could occur between isostructural vanadates and manganites in both 113-type and 214-type superlattices. The charge transfer is enhanced by associated lattice distortions. The moderate electronegativity difference between Mn and V leads to moderate charge transfer, in contrast to the LaTiO<sub>3</sub>/LaNiO<sub>3</sub> superlattice, in which a complete charge transfer fills up the holes on the oxygen atoms in the NiO<sub>2</sub> layer [74]. The partially filled bands imply metallic conductance that could possibly be observed in transport, if the thin film quality is high enough that disorder is suppressed and Anderson localization does not occur [75]. Our study of a superlattice consisting of two different species of transition-metal oxides establishes that internal charge transfer is a powerful tool to engineer electronic structure and tailor correlation effects in transition-metal oxides [29,76]. In particular, for vanadate-manganite superlattices, internal charge transfer may serve as an alternative approach to dope Mott insulators without introducing chemical disorder. Furthermore, as previous works have shown [77,78], in addition to perovskite structure, Ruddlesden-Popper structures can also be an important ingredient in the design of oxide superlattices with tailored properties [79]. Finally, our examination of different materials raises the issue of the value of the double-counting coefficient  $U'$ , determined here by fitting photoemission data. Understanding the variation of  $U'$  across the transition-metal oxide family of materials is an important open problem.

## ACKNOWLEDGMENTS

We are grateful to Darrell Schlom, Kyle Shen, Eric Monkman, and Masaki Uchida for stimulating discussion and sharing the unpublished data with us. H.C. is supported by National Science Foundation under Grant No. DMR-1120296. A.J.M. is supported by the Department of Energy under Grant No. DOE-ER-046169. H.P. and C.A.M. are supported by FAME, one of six centers of STARnet, a Semiconductor Research Corporation program sponsored by MARCO and DARPA. Computational facilities are provided via XSEDE resources through Grant No. TG-PHY130003.

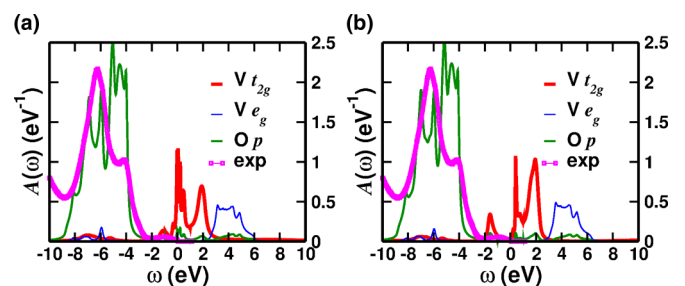


FIG. 7. (Color online) Orbitaly resolved spectral function of Sr<sub>2</sub>VO<sub>4</sub>, obtained from LDA+DMFT calculations.  $U'$  double counting is employed with (a)  $U_V = 5$  eV,  $U'_V = 3.5$  eV and (b) with  $U_V = 8$  eV,  $U'_V = 6.8$  eV. The red (very thick), blue (thick) and green (thin) curves are V  $t_{2g}$ , V  $e_g$  and O  $p$  projected spectral functions, respectively. The pink dots are experimental photoemission data for SrVO<sub>3</sub> [61]. The Fermi level is set at zero energy.

### APPENDIX A: METAL-INSULATOR TRANSITION OF $\text{Sr}_2\text{VO}_4$

In this Appendix, we show that within single-site DMFT and with the  $p$ - $d$  separation fixed by the experimental photoemission data, there is a metal-insulator transition in  $\text{Sr}_2\text{VO}_4$  with an increasing Hubbard  $U_V$  ( $U'_V$  is determined by the  $p$ - $d$  separation for each given  $U_V$ ). Figure 7(a) shows that for  $U_V = 5$  eV and  $U'_V = 3.5$  eV,  $\text{Sr}_2\text{VO}_4$  is metallic with mainly V  $t_{2g}$  states at the Fermi level, which is a reproduction of Fig. 3(b). Figure 7(b) shows that with  $U_V$  increased to 8 eV and  $U'_V$  to 6.8 eV which approximately fixes the  $p$ - $d$  separation, a metal-insulator transition occurs and  $\text{Sr}_2\text{VO}_4$  is rendered a Mott insulator. However, the critical  $U_V$  depends on the approximation scheme we employ. A more elaborate cluster-DMFT calculation and/or the inclusion of long-range order may find a smaller critical  $U_V$  [72].

### APPENDIX B: MOTT GAP OF $\text{Sr}_2\text{MnO}_4$ AND ITS EFFECTS ON $\text{Sr}_2\text{MnO}_4/\text{Sr}_2\text{VO}_4$ SUPERLATTICES

In this Appendix, we show how the Hubbard  $U_{\text{Mn}}$  changes the Mott gap of  $\text{Sr}_2\text{MnO}_4$  with the  $p$ - $d$  separation approximately fixed. Figure 8(a) shows the orbitally resolved spectral function of  $\text{Sr}_2\text{MnO}_4$  with  $U_{\text{Mn}} = 8$  eV and  $U'_{\text{Mn}} = 7.5$  eV. Note that since  $\text{Sr}_2\text{MnO}_4$  is a Mott insulator, the Fermi level in the calculation is shifted at the conduction band edge, i.e.,

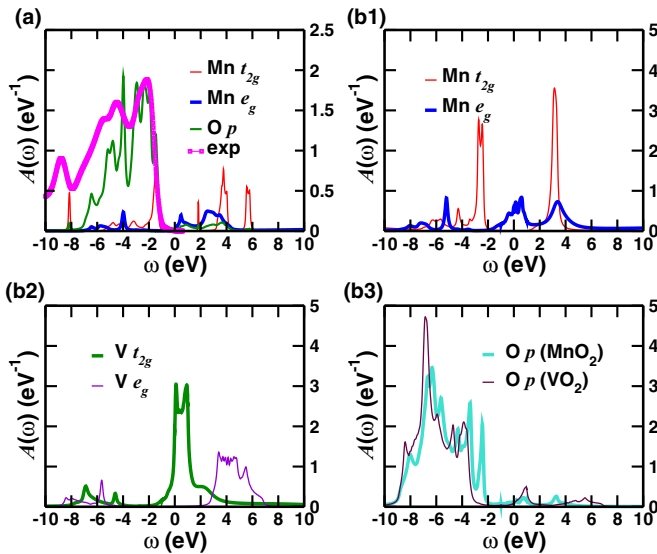


FIG. 8. (Color online) (a) Orbitally resolved spectral function of  $\text{Sr}_2\text{MnO}_4$ , obtained from LDA+DMFT calculations.  $U'$  double counting is employed with  $U_{\text{Mn}} = 8$  eV,  $U'_{\text{Mn}} = 7.5$  eV. The red (thin), blue (very thick), and green curves (thick) are Mn  $t_{2g}$ , Mn  $e_g$ , and O  $p$  projected spectral functions, respectively. The pink dots are experimental photoemission data of  $\text{SrMnO}_3$  [61]. The Fermi level is set at zero energy. (b) Orbitally resolved spectral function of  $\text{Sr}_2\text{VO}_4/\text{Sr}_2\text{MnO}_4$  superlattices, obtained from LDA+DMFT calculations.  $U'$  double counting is employed with  $U_{\text{Mn}} = 8$  eV,  $U'_{\text{Mn}} = 7.5$  eV, and  $U_V = 5$  eV,  $U'_V = 3.5$  eV. (b1) Mn  $t_{2g}$  (red thin) and Mn  $e_g$  (blue thick) states; (b2) V  $t_{2g}$  (green thick) and V  $e_g$  (violet thin) states; (b3) O  $p$  states of the  $\text{MnO}_2$  layer (turquoise thick) and O  $p$  states of the  $\text{VO}_2$  layer (maroon thin).

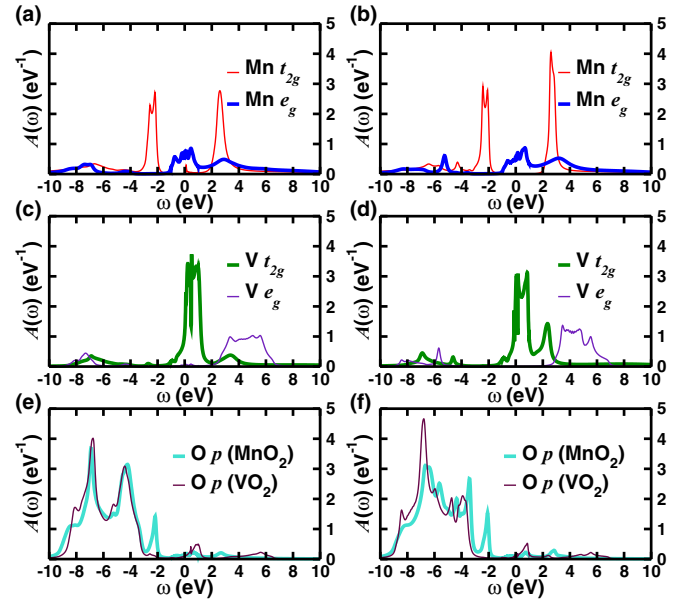


FIG. 9. (Color online) Orbitally resolved spectral function of vanadate-manganite superlattices, obtained from LDA+DMFT calculations. Left:  $\text{SrVO}_3/\text{SrMnO}_3$  superlattice. Right:  $\text{Sr}_2\text{VO}_4/\text{Sr}_2\text{MnO}_4$  superlattice. (a) and (b) Mn  $t_{2g}$  (red thin) and Mn  $e_g$  (blue thick) states; (c) and (d) V  $t_{2g}$  (green thick) and V  $e_g$  (violet thin) states; (e) and (f) O  $p$  states of the  $\text{MnO}_2$  layer (turquoise thick) and O  $p$  states of the  $\text{VO}_2$  layer (maroon thin). Fully localized limit double counting is employed with  $U_V = U_{\text{Mn}} = 5$  eV. The Fermi level is set at zero energy.

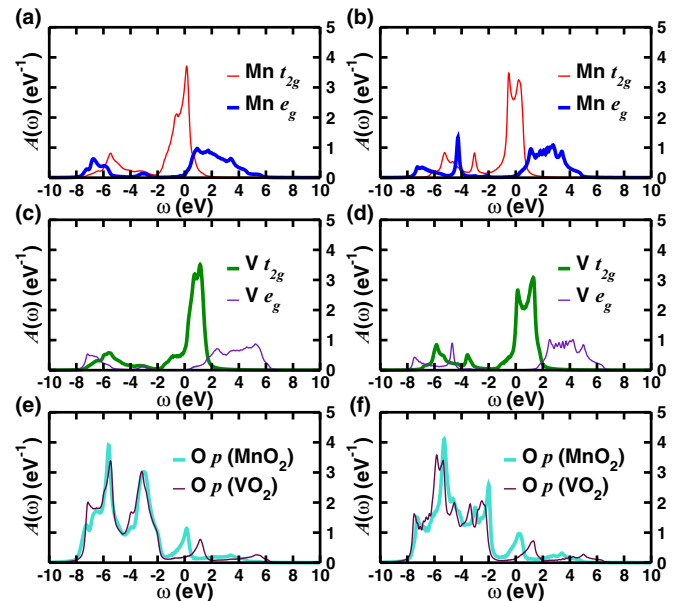


FIG. 10. (Color online) Orbitally resolved spectral function of vanadate-manganite superlattices, obtained from LDA calculations. Left:  $\text{SrVO}_3/\text{SrMnO}_3$  superlattice. Right:  $\text{Sr}_2\text{VO}_4/\text{Sr}_2\text{MnO}_4$  superlattice. (a) and (b) Mn  $t_{2g}$  (red thin) and Mn  $e_g$  (blue thick) states; (c) and (d) V  $t_{2g}$  (green thick) and V  $e_g$  (violet thin) states; (e) and (f) O  $p$  states of the  $\text{MnO}_2$  layer (turquoise thick) and O  $p$  states of the  $\text{VO}_2$  layer (maroon thin).

TABLE III. The occupancy of V  $d$  and Mn  $d$  states, as well as VO<sub>2</sub> and MnO<sub>2</sub> layers in vanadates, manganites and the superlattices. All the occupancies without the parentheses are calculated from Wannier basis using the DFT-LDA relaxed structures. The occupancies in the parentheses are calculated from Wannier basis using the experimental structures.

SrVO <sub>3</sub>	SrMnO <sub>3</sub>	(SrVO <sub>3</sub> ) <sub>1</sub> /(SrMnO <sub>3</sub> ) <sub>1</sub>		(SrVO <sub>3</sub> ) <sub>2</sub> /(SrMnO <sub>3</sub> ) <sub>2</sub>	
$N_d(\text{V})$	$N_d(\text{Mn})$	$N_d(\text{V})$	$N_d(\text{Mn})$	$N_d(\text{V})$	$N_d(\text{Mn})$
2.09 (2.03)	4.08 (4.06)	1.73	4.51	1.69	4.54
$N(\text{VO}_2)$	$N(\text{MnO}_2)$	$N(\text{VO}_2)$	$N(\text{MnO}_2)$	$N(\text{VO}_2)$	$N(\text{MnO}_2)$
13.36 (13.34)	15.36 (15.35)	12.86	15.92	12.82	15.95

the edge of Mn  $e_g$  states. In Fig. 3(d) of the main text, the Mott gap of Sr<sub>2</sub>MnO<sub>4</sub> is around 0.5 eV with  $U_{\text{Mn}} = 5$  eV and  $U'_{\text{Mn}} = 4.5$  eV. If we increase  $U_{\text{Mn}}$  to 8 eV and  $U'_{\text{Mn}}$  to 7.5 eV, the Mott gap is correspondingly increased to around 1 eV with the  $p$ - $d$  separation fixed by the photoemission data [61]. The Mn  $t_{2g}$  peak and the main peak of O  $p$  states now merge together. However, even with  $U_{\text{Mn}} = 8$  eV, the Mott gap is still smaller than the optical gap (around 2 eV) from experiment [30]. The difference could be due to spatial correlations not included in our single-site DMFT approximation [72].

Using the parameters  $U_{\text{Mn}} = 8$  eV and  $U'_{\text{Mn}} = 7.5$  eV, we redo the calculations on Sr<sub>2</sub>VO<sub>4</sub>/Sr<sub>2</sub>MnO<sub>4</sub> superlattices (with  $U_{\text{V}} = 5$  eV and  $U'_{\text{V}} = 3.5$  eV) to test the effects of Mott gap size on charge transfer. As Fig. 8(b) shows, the key features in electronic structure remain the same as Fig. 4 in the main text: (i) Mn  $e_g$  and V  $t_{2g}$  states emerge at the Fermi level and (ii) the main peaks of O  $p$  states associated with the MnO<sub>2</sub> and VO<sub>2</sub> layers are approximately aligned. This shows that it is the  $p$ - $d$  separation that controls the charge transfer across the interface while the size of Mott gap plays a secondary role.

#### APPENDIX C: ELECTRONIC STRUCTURE CALCULATED USING THE FULLY LOCALIZED LIMIT DOUBLE COUNTING

In this Appendix, we show the electronic structure of both SrVO<sub>3</sub>/SrMnO<sub>3</sub> and Sr<sub>2</sub>VO<sub>4</sub>/Sr<sub>2</sub>MnO<sub>4</sub> superlattices, calcu-

lated using the standard fully localized limit (FLL) double counting. The orbitally resolved spectral function is shown in Fig. 9, which is compared to Fig. 4 in the main text. We employ  $U_{\text{V}} = U_{\text{Mn}} = 5$  eV. We find the FLL double counting does not change the key features of electronic structure, such as the emergence of Mn  $e_g$  and V  $t_{2g}$  states at the Fermi level.

#### APPENDIX D: ELECTRONIC STRUCTURE CALCULATED USING THE LOCAL DENSITY APPROXIMATION

In this Appendix, we show the electronic structure of both SrVO<sub>3</sub>/SrMnO<sub>3</sub> and Sr<sub>2</sub>VO<sub>4</sub>/Sr<sub>2</sub>MnO<sub>4</sub> superlattices, calculated using the local density approximation alone. The orbitally resolved spectral function is shown in Fig. 10, which is compared to Fig. 4 in the main text. We illustrate that without including strong correlation effect via Hubbard  $U$ , Mn  $t_{2g}$  states lie around the Fermi level and do not split into lower and upper Hubbard bands.

#### APPENDIX E: (SrVO<sub>3</sub>)<sub>1</sub>/(SrMnO<sub>3</sub>)<sub>1</sub> VERSUS (SrVO<sub>3</sub>)<sub>2</sub>/(SrMnO<sub>3</sub>)<sub>2</sub> SUPERLATTICES

In this Appendix, we compare the (SrVO<sub>3</sub>)<sub>1</sub>/(SrMnO<sub>3</sub>)<sub>1</sub> superlattice to the (SrVO<sub>3</sub>)<sub>2</sub>/(SrMnO<sub>3</sub>)<sub>2</sub> superlattice. We focus on the  $d$  occupancy and the charge transfer from V to Mn sites. Table III shows that  $N_d$  of V sites and Mn sites are very similar between (SrVO<sub>3</sub>)<sub>1</sub>/(SrMnO<sub>3</sub>)<sub>1</sub> and (SrVO<sub>3</sub>)<sub>2</sub>/(SrMnO<sub>3</sub>)<sub>2</sub> superlattices.

- [1] A. Ohtomo, D. A. Muller, J. L. Grazul, and H. Y. Hwang, *Nature (London)* **419**, 378 (2002).
- [2] S. Okamoto and A. J. Millis, *Nature (London)* **428**, 630 (2004).
- [3] P. Moetakef, J. Y. Zhang, A. Kozhanov, B. Jalan, R. Seshadri, S. J. Allen, and S. Stemmer, *Appl. Phys. Lett.* **98**, 112110 (2011).
- [4] A. Ohtomo and H. Y. Hwang, *Nature (London)* **427**, 423 (2004).
- [5] S. Thiel, G. Hammerl, A. Schmehl, C. W. Schneider, and J. Mannhart, *Science* **313**, 1942 (2006).
- [6] N. Reyren, S. Thiel, A. D. Caviglia, L. F. Kourkoutis, G. Hammerl, C. Richter, C. W. Schneider, T. Kopp, A. S. Rüetschi, D. Jaccard *et al.*, *Science* **317**, 1196 (2007).
- [7] A. D. Caviglia, S. Gariglio, N. Reyren, D. Jaccard, T. Schneider, M. Gabay, S. Thiel, G. Hammerl, J. Mannhart, and J. M. Triscone, *Nature (London)* **456**, 624 (2008).
- [8] T. Koida, M. Lippmaa, T. Fukumura, K. Itaka, Y. Matsumoto, M. Kawasaki, and H. Koinuma, *Phys. Rev. B* **66**, 144418 (2002).
- [9] S. Smadici, P. Abbamonte, A. Bhattacharya, X. Zhai, B. Jiang, A. Rusydi, J. N. Eckstein, S. D. Bader, and J.-M. Zuo, *Phys. Rev. Lett.* **99**, 196404 (2007).
- [10] B. R. K. Nanda and S. Satpathy, *Phys. Rev. Lett.* **101**, 127201 (2008).
- [11] A. Brinkman, M. Huijben, M. V. Zalk, J. Huijben, U. Zeitler, J. C. Maan, W. G. V. der Wiel, G. Rijnders, D. H. A. Blank, and H. Hilgenkamp, *Nat. Mater.* **6**, 493 (2007).
- [12] J. A. Bert, B. Kalisky, C. Bell, M. Kim, Y. Hikita, H. Y. Hwang, and K. A. Moler, *Nat. Phys.* **7**, 767 (2011).
- [13] L. Li, C. Richter, J. Mannhart, and R. C. Ashoori, *Nat. Phys.* **7**, 762 (2011).
- [14] J. Chakhalian, J. W. Freeland, H.-U. Habermeier, G. Cristiani, G. Khaliullin, M. van Veenendaal, and B. Keimer, *Science* **318**, 1115 (2007).

- [15] E. Benckiser, M. W. Haverkort, S. Brück, E. Goering, S. Macke, A. Frañó, X. Yang, O. K. Andersen, G. Cristiani, H.-U. Habermeier *et al.*, *Nat. Mater.* **10**, 189 (2011).
- [16] H. Y. Hwang, *Science* **313**, 1895 (2006).
- [17] Y. Tokura and H. Hwang, *Nat. Mater.* **7**, 694 (2008).
- [18] J. Mannhart and D. G. Schlom, *Science* **327**, 1607 (2010).
- [19] J. Chakhalian, A. J. Millis, and J. Rondinelli, *Nat. Mater.* **11**, 92 (2012).
- [20] N. Nakagawa, H. Y. Hwang, and D. A. Muller, *Nat. Mater.* **5**, 204 (2006).
- [21] J. S. Lee, Y. W. Xie, H. K. Sato, C. Bell, Y. Hikita, H. Y. Hwang, and C. C. Kao, *Nat. Mater.* **12**, 703 (2013).
- [22] J. Mannhart, D. H. A. Blank, H. Y. Hwang, A. J. Millis, and J. M. Triscone, *MRS Bull.* **33**, 1027 (2008).
- [23] M. Huijben, A. Brinkman, G. Koster, G. Rijnders, H. Hilgenkamp, and D. H. A. Blank, *Adv. Mater.* **21**, 1665 (2009).
- [24] H. Chen, A. M. Kolpak, and S. Ismail-Beigi, *Adv. Mater.* **22**, 2881 (2010).
- [25] P. Zubko, S. Gariglio, M. Gabay, P. Ghosez, and J.-M. Triscone, *Ann. Rev. Condens. Matter Phys.* **2**, 141 (2011).
- [26] M. B. Salamon and M. Jaime, *Rev. Mod. Phys.* **73**, 583 (2001).
- [27] A. Moreo, M. Mayr, A. Feiguin, S. Yunoki, and E. Dagotto, *Phys. Rev. Lett.* **84**, 5568 (2000).
- [28] A. Bhattacharya, S. J. May, S. G. E. te Velthuis, M. Warusawithana, X. Zhai, B. Jiang, J.-M. Zuo, M. R. Fitzsimmons, S. D. Bader, and J. N. Eckstein, *Phys. Rev. Lett.* **100**, 257203 (2008).
- [29] H. Chen, A. J. Millis, and C. A. Marianetti, *Phys. Rev. Lett.* **111**, 116403 (2013).
- [30] J. Matsuno, Y. Okimoto, M. Kawasaki, and Y. Tokura, *Phys. Rev. Lett.* **95**, 176404 (2005).
- [31] R. Søndena, P. Ravindran, S. Stølen, T. Grande, and M. Hanfland, *Phys. Rev. B* **74**, 144102 (2006).
- [32] H. T. Dang, A. J. Millis, and C. A. Marianetti, *Phys. Rev. B* **89**, 161113 (2014).
- [33] P. Hohenberg and W. Kohn, *Phys. Rev.* **136**, B864 (1964).
- [34] W. Kohn and L. J. Sham, *Phys. Rev.* **140**, A1133 (1965).
- [35] A. Georges, G. Kotliar, W. Krauth, and M. J. Rozenberg, *Rev. Mod. Phys.* **68**, 13 (1996).
- [36] G. Kotliar, S. Y. Savrasov, K. Haule, V. S. Oudovenko, O. Parcollet, and C. A. Marianetti, *Rev. Mod. Phys.* **78**, 865 (2006).
- [37] M. C. Payne, M. P. Teter, D. C. Allan, T. A. Arias, and J. D. Joannopoulos, *Rev. Mod. Phys.* **64**, 1045 (1992).
- [38] G. Kresse and J. Hafner, *Phys. Rev. B* **47**, 558 (1993).
- [39] G. Kresse and J. Hafner, *J. Phys.: Condens. Matter* **6**, 8245 (1994).
- [40] G. Kresse and J. Furthmüller, *Comp. Mater. Sci.* **6**, 15 (1996).
- [41] G. Kresse and J. Furthmüller, *Phys. Rev. B* **54**, 11169 (1996).
- [42] P. E. Blöchl, *Phys. Rev. B* **50**, 17953 (1994).
- [43] G. Kresse and D. Joubert, *Phys. Rev. B* **59**, 1758 (1999).
- [44] J. P. Perdew and A. Zunger, *Phys. Rev. B* **23**, 5048 (1981).
- [45] J. P. Perdew, K. Burke, and M. Ernzerhof, *Phys. Rev. Lett.* **77**, 3865 (1996).
- [46] N. Marzari, A. A. Mostofi, J. R. Yates, I. Souza, and D. Vanderbilt, *Rev. Mod. Phys.* **84**, 1419 (2012).
- [47] The average spread per Wannier function for each constituent is: LDA–0.75 Å<sup>2</sup> for SrVO<sub>3</sub>, 0.80 Å<sup>2</sup> for SrMnO<sub>3</sub>, 0.96 Å<sup>2</sup> for Sr<sub>2</sub>VO<sub>4</sub> and 0.83 Å<sup>2</sup> for Sr<sub>2</sub>MnO<sub>4</sub>; GGA–0.73 Å<sup>2</sup> for SrVO<sub>3</sub>, 0.78 Å<sup>2</sup> for SrMnO<sub>3</sub>, 0.93 Å<sup>2</sup> for Sr<sub>2</sub>VO<sub>4</sub> and 0.90 Å<sup>2</sup> for Sr<sub>2</sub>MnO<sub>4</sub>.
- [48] X. Wang, M. J. Han, L. de' Medici, H. Park, C. A. Marianetti, and A. J. Millis, *Phys. Rev. B* **86**, 195136 (2012).
- [49] H. Park, A. J. Millis, and C. A. Marianetti, *Phys. Rev. B* **89**, 245133 (2014).
- [50] E. Pavarini, S. Biermann, A. Poteryaev, A. I. Lichtenstein, A. Georges, and O. K. Andersen, *Phys. Rev. Lett.* **92**, 176403 (2004).
- [51] I. A. Nekrasov, G. Keller, D. E. Kondakov, A. V. Kozhevnikov, T. Pruschke, K. Held, D. Vollhardt, and V. I. Anisimov, *Phys. Rev. B* **72**, 155106 (2005).
- [52] M. Aichhorn, L. Pourovskii, V. Vildosola, M. Ferrero, O. Parcollet, T. Miyake, A. Georges, and S. Biermann, *Phys. Rev. B* **80**, 085101 (2009).
- [53] J.-H. Park, C. T. Chen, S.-W. Cheong, W. Bao, G. Meigs, V. Chakarian, and Y. U. Idzerda, *Phys. Rev. Lett.* **76**, 4215 (1996).
- [54] P. Werner, A. Comanac, L. de' Medici, M. Troyer, and A. J. Millis, *Phys. Rev. Lett.* **97**, 076405 (2006).
- [55] P. Werner and A. J. Millis, *Phys. Rev. B* **74**, 155107 (2006).
- [56] K. Haule, *Phys. Rev. B* **75**, 155113 (2007).
- [57] E. Gull, A. J. Millis, A. I. Lichtenstein, A. N. Rubtsov, M. Troyer, and P. Werner, *Rev. Mod. Phys.* **83**, 349 (2011).
- [58] H. Chen, A. J. Millis, and C. A. Marianetti (unpublished).
- [59] M. T. Czyżyk and G. A. Sawatzky, *Phys. Rev. B* **49**, 14211 (1994).
- [60] In addition to the FLL and  $U'$  double-counting formulas, other double-counting schemes also exist, such as the around mean field (AMF) limit:  $V_{dc} = \frac{9}{10}(U - 2J)N_d - \frac{1}{5}JN_d$  [59].
- [61] Eric Monkman, Masaki Uchida, Kyle Shen, and Darrell Schlom (unpublished).
- [62] T. Maekawa, K. Kurosaki, and S. Yamanaka, *J. Alloys Compd.* **426**, 46 (2006).
- [63] H. D. Zhou, B. S. Conner, L. Balicas, and C. R. Wiebe, *Phys. Rev. Lett.* **99**, 136403 (2007).
- [64] J. Teyssier, R. Viennois, E. Giannini, R. M. Eremina, A. Günther, J. Deisenhofer, M. V. Eremin, and D. van der Marel, *Phys. Rev. B* **84**, 205130 (2011).
- [65] E. Gull, M. Ferrero, O. Parcollet, A. Georges, and A. J. Millis, *Phys. Rev. B* **82**, 155101 (2010).
- [66] R. Søndena, S. Stølen, P. Ravindran, and T. Grande, *Phys. Rev. B* **75**, 214307 (2007).
- [67] K. Tezuka, M. Inamura, Y. Hinatsu, Y. Shimojo, and Y. Morii, *J. Solid State Chem.* **145**, 705 (1999).
- [68] Due to the insulating nature, the theoretical Fermi level of both SrMnO<sub>3</sub> and Sr<sub>2</sub>MnO<sub>4</sub> is shifted to the Mn conduction band edge, and is aligned with the experimental Fermi level when the spectral function and the photoemission data are compared.
- [69] T. Saitoh, A. E. Bocquet, T. Mizokawa, H. Namatame, A. Fujimori, M. Abbate, Y. Takeda, and M. Takano, *Phys. Rev. B* **51**, 13942 (1995).
- [70] G. Zampieri, F. Prado, A. Caneiro, J. Briático, M. T. Causa, M. Tovar, B. Alascio, M. Abbate, and E. Morikawa, *Phys. Rev. B* **58**, 3755 (1998).
- [71] T. Saitoh, A. E. Bocquet, T. Mizokawa, H. Namatame, A. Fujimori, M. Abbate, Y. Takeda, and M. Takano, *Jpn. J. Appl. Phys.* **32** (Suppl. 32-3), 258 (1993).
- [72] A. Go and A. J. Millis, *Phys. Rev. Lett.* (to be published).

- [73] The explicit definition of  $\overline{\Delta N_d}$  is  $\overline{\Delta N_d} = \frac{1}{2}(|N_d(\text{V}_{\text{bulk}}) - N_d(\text{V}_{\text{superlattice}})| + |N_d(\text{Mn}_{\text{bulk}}) - N_d(\text{Mn}_{\text{superlattice}})|)$ .  $\overline{\Delta N}$  uses a similar definition.
- [74] The electronegativity  $\chi$  of V in SrVO<sub>3</sub> and Mn in SrMnO<sub>3</sub> can be estimated by employing the Wannier functions to calculate the  $p$ - $d$  separation. Among the three O  $p$  states, using the one with the highest onsite energy, and the relevant transition-metal  $d$  states, we find that in SrVO<sub>3</sub>,  $\chi(\text{V-}t_{2g}) = -3.13$  eV and in SrMnO<sub>3</sub>  $\chi(\text{Mn-}e_g) = -2.99$  eV. Therefore  $\chi(\text{Mn-}e_g) \frac{1}{4} \chi(\text{V-}t_{2g}) = 0.14$  eV > 0, leading to a moderate charge transfer from V to Mn. Applying the same methods to LaNiO<sub>3</sub> and LaTiO<sub>3</sub>, we find that  $\chi(\text{Ni-}e_g) - \chi(\text{Ti-}t_{2g}) = 2.93$  eV, leading a complete charge transfer from Ti to Ni.
- [75] P. A. Lee and T. V. Ramakrishnan, *Rev. Mod. Phys.* **57**, 287 (1985).
- [76] J. E. Kleibecker, Z. Zhong, H. Nishikawa, J. Gabel, A. Müller, F. Pfaff, M. Sing, K. Held, R. Claessen, G. Koster *et al.*, *Phys. Rev. Lett.* **113**, 237402 (2014).
- [77] H. Akamatsu, K. Fujita, T. Kuge, A. Sen Gupta, A. Togo, S. Lei, F. Xue, G. Stone, J. M. Rondinelli, L.-Q. Chen *et al.*, *Phys. Rev. Lett.* **112**, 187602 (2014).
- [78] A. T. Mulder, N. A. Benedek, J. M. Rondinelli, and C. J. Fennie, *Adv. Funct. Mater.* **23**, 4810 (2013).
- [79] C.-H. Lee, N. D. Orloff, T. Birol, Y. Zhu, V. Goian, E. Rocas, R. Haislmaier, E. Vlahos, J. A. Mundy, L. F. Kourkoutis *et al.*, *Nature (London)* **502**, 532 (2013).